Liu, J., et al., 2021, Isotopically “heavy” pyrite in marine sediments due to high sedimentation rates and non-steady-state deposition: Geology, v. 49, https://doi.org/10.1130/G48415.1

SUPPLEMENTAL MATERIAL: Liu et al. Isotopically ‘heavy’ pyrite in marine sediments due to high sedimentation rates and non-steady-state deposition.

GEOLOGICAL BACKGROUND

Located in the southwestern sector of the Baltic Sea, the Bornholm Basin is a half-graben bound by major faults (Jensen et al., 2017). Typifying the Bornholm Basin fill as a whole, the sediment cores examined herein comprise grey Holocene-aged muds in their upper reaches that succeed light-brown clays at variable core depths (4.2–9.6 mbsf; Table S1). This distinctive lithological change marks the post-glacial marine transgression that culminated in the transition between the Ancylus Lake and the Littorina Sea stages that typify the evolution of the wider Baltic basin (Andrén et al., 2000; Hilligsøe et al., 2018). Here, as sea level rose in the wake of the last glaciation, organic-rich and sulfidic Littorina Sea muds started to accumulate at ca. 8.5 ka BP. The thickness of these muds was influenced by the underlying topography, inducing significant spatial variability in the thickness and accumulation rates of what is generalized as the Holocene Mud Layer (HML; Table S1; Hilligsøe et al., 2018). Consequently, the HML deposits are thickest near the fault scarp in the southwestern part of the basin and thin towards the central and deepest parts of the basin in the northeast (Jensen et al., 2017). Once the Öresund and Great Belt Straits were breached, continuous seawater inflow coupled with post-glacial warming increased primary productivity and the development of water-column stratification, combining to enhance the preservation of sedimentary organic matter, manifest as elevated total organic carbon contents (Figs. S1D, S3A; Andrén et al., 2000; Liu et al., 2020).

The vertical distribution of sulfate and methane within the sedimentary fill of the Bornholm Basin is modulated by the thickness of the HML (Table S1). For instance, within Aarhus Bay,

Flury et al. (2016) demonstrated that both the rates of methanogenesis and the upward flux of methane are positively related to the thickness of the underlying organic-rich strata. Here, heightened methane fluxes trigger a shoaling of the sulfate-methane transition (SMT), exposing sediment with more reactive organic matter to methanogenesis, thereby enhancing methane production. Such positive feedback is also seen in the Bornholm Basin and is responsible for the marked differences seen in SMT depths across the basin (Hilligsøe et al., 2018).

SUPPLEMENTAL MATERIALS AND METHODS

Site Description

Sediment cores at sites BB01, BB02, BB03 and BB05 were taken at water depths of 84–96 m during a research cruise on the R/V *Aurora* in 2016 (Table S1). Each site was sampled with a gravity corer (9 m in length) and a Rumohr corer (1 m in length). Site BB03 represents a reoccupation of site M0065, cored during Expedition 347 of the Integrated Ocean Drilling Program (Andrén et al., 2015). Herein we focus on the upper few meters (< 5 m) of Holocene-aged grey-colored mud with an average porosity of 0.86 ± 0.06 (1σ; Beulig et al., 2018). Biostratigraphic and seismo-acoustic markers (Beulig et al., 2018) show that these marine-derived sediments record constant sedimentation extending for 8.5 ka. Similarly, the three neighboring cores (BB01, BB02 and BB05) record constant sedimentation, albeit with lower sedimentation rates (Beulig et al., 2018).

Porewater Sampling and Analysis

Sampling and analytical protocols employed herein have been detailed previously (Beulig et al., 2018; Liu et al., 2020; Pellerin et al., 2018) and, therefore, are only briefly summarized.

Porewater samples were collected in Vacutainers® via the direct insertion of Rhizon soil moisture samplers. Aliquots of porewater samples were subsequently split for the following analytical assays. Samples reserved for porewater sulfate analysis were purged with humidified CO_2, removing H_2S, permitting sulfate quantification by ion chromatography using a Dionex IC system equipped with an AG-18/AS-18 column and a KOH eluent. Aqueous sulfide ($\sum H_2S$) was fixed with 5% (wt./vol.) zinc acetate solution and quantified spectrophotometrically by the methylene blue method (Cline, 1969). Dissolved iron concentrations were measured using a Thermo Fisher Scientific Element 2 inductively coupled plasma-mass spectrometer (ICP-MS) after dilution with 0.01 N nitric acid. Samples for methane analysis were taken immediately upon core retrieval and transferred to glass vials containing a saturated NaCl solution. Headspace concentrations were determined by flame ionization gas chromatography (SRI 310C; SRI Instruments) after separation on a packed silica gel column.

Solid-phase Sediment Sampling and Analysis

Sediments were subsampled immediately after recovery under oxygen-free conditions. Cut-off syringes were used to collect push samples, which were sealed with Parafilm™ and immediately frozen at −20 °C. In the laboratory, frozen sediment samples were submerged in 5% (wt./vol.) zinc acetate solution. Zero-valent sulfur (ZVS), predominantly elemental sulfur, was then extracted from the defrosted samples via sustained agitation (~15 hours) in a mixed 3:1 methanol:toluene solution. Following separation from the solid residue, ZVS concentrations were determined by UV detection at 230 nm after separation by reversed-phase high-performance liquid chromatography (HPLC) using a C-18 column (Findlay et al., 2014). The detection limit of this approach was 0.5 µM.

The ZVS from the supernatant was converted to sulfide by treatment with hot acidified $CrCl_2$ solution. The solid residue was treated sequentially with cold 6N HCl, yielding Acid Volatile Sulfur (AVS, predominantly Fe monosulfide), and then with hot acidified $CrCl_2$ solution, yielding Chromium Reducible Sulfur (CRS, mainly pyrite; Fossing and Jørgensen, 1989). The sulfide evolved from these extractions was flushed within a N_2 stream through 5% (wt./vol.) zinc acetate solution and trapped as ZnS. The AVS and CRS contents were determined spectrophotometrically (672 nm) by the methylene blue method (Cline, 1969). Finally, the ZVS-, AVS- and CRS-derived ZnS was converted to Ag_2S via reaction with $AgNO_3$ and cleaned prior to sulfur isotope analysis.

Sequential iron extractions followed a protocol modified from Poulton and Canfield (2005) and Henkel et al. (2016) using ~50 mg of dry sediment and 5 mL of the following extractants: (i) Na-acetate to dissolve Fe-carbonates (Fe_{aca}), (ii) hydroxylamine-HCl to dissolve easily reducible Fe-oxides (Fe_{hyam}), (iii) Na-dithionite/citrate to dissolve reducible Fe-oxides ($Fe_{di\text{-}ct}$), and (iv) ammonium oxalate/oxalic acid to dissolve magnetite (Fe_{oxa}). The iron content of these extracts was analyzed at the Alfred Wegener Institute Helmholtz Centre for Polar and Marine Research by inductively coupled plasma-optical emission spectrometry (ICP-OES; Thermo Fisher Scientific iCAP 7400). Replicate analyses of standards (MESS-4 and He443-77cc) showed a relative standard deviation (RSD) of better than 6%. Given that AVS is quantitatively extracted during the acetate extractions (Poulton and Canfield, 2005), the Fe_{aca} content is reported as the difference between the acetate and the AVS extractions. After correction, the highly reactive iron content (Fe_{HR}) of a sample is defined as the sum of the Fe_{AVS}, Fe_{py}, Fe_{aca}, Fe_{hyam}, $Fe_{di\text{-}ct}$ and Fe_{oxa} pools. Furthermore, the extent of pyritization of the highly reactive iron pool is assessed by normalizing the iron content in pyrite (Fe_{py}) to Fe_{HR} (i.e., Fe_{py}/Fe_{HR}), where Fe_{py} is calculated from the measured CRS content assuming a Fe:S stoichiometry of 1:2. To better distinguish the relative

fractions of poorly versus highly crystalline Fe minerals, we quantified non-sulfur-bound reactive iron in two different ways: (i) the sum of Fe_{aca} and Fe_{hyam} and (ii) the sum of Fe_{aca}, Fe_{hyam}, $Fe_{di\text{-}ct}$ and Fe_{oxa} (Fig. S1F; Liu et al., 2020). In Figs. 2C and 3C, the oxalate extraction has been excluded owing to its ability to liberate iron from clays (Slotznick et al., 2020), which are anticipated to be unreactive toward sulfide over timescales relevant to this study (Canfield et al., 1992). All solid-phase iron and sulfur data are reported relative to the wet mass of the sediment.

Total organic carbon (TOC) contents, reported in dry weight percent, were determined by flash combustion of acid-treated carbonate-free residues using a Carlo Erba NA-1500 CN analyzer with an RSD of ~2%. Density was determined using wet sample masses and volumes and is expressed as the wet weight in g per cm^3. Porewater methane, sulfate, sulfide and TOC concentrations at site BB03 were published previously (Beulig et al., 2018; Pellerin et al., 2018).

Sulfur Isotope Analysis

Sulfate and sulfide in porewaters were precipitated as barium sulfate and silver sulfide, respectively. For major S-isotope determination ($\delta^{34}S$; Equ. 1) after cleaning, these dried precipitates were weighed into tin cups with a combustion catalyst (V_2O_5) and converted to SO_2 via flash combustion at 1030°C using a Flash Element Analyzer. The isotopic composition was determined online by continuous-flow gas-source isotope-ratio mass spectrometry using a Thermo Finnegan Delta V Plus in the Godwin Laboratory for Paleoclimate Research at the University of Cambridge. For multiple sulfur isotope analysis, 2–3 mg aliquots of Ag_2S were converted to SF_6 by overnight exposure to a 100 Torr F_2 atmosphere at 300°C in the Laboratory of Stable Isotope Geobiology at Massachusetts Institute of Technology. Following automated cryogenic and gas chromatographic separation, the purified SF_6 was transferred into an evacuated multi-port on a

designated Thermo MAT 253 isotope-ratio mass spectrometer operated in dual-inlet mode (Ono et al., 2012).

Following convention, major sulfur isotope data are reported in standard delta-notation:

$$\delta^{3X}S\ (‰) = [(^{3X}R_{Sample}/^{3X}R_{VCDT}) - 1] \times 1000 \quad (1)$$

while the minor sulfur isotopic data are presented in capital-delta notation:

$$\Delta^{33}S\ (‰) = \delta^{33}S - 1000 \times [(1 + \delta^{34}S/1000)^{0.515} - 1] \quad (2)$$

Here, $^{3X}R_{Sample}/^{3X}R_{VCDT}$ is the sulfur isotopic ratio of a sample ($^{3X}R_{Sample} = {}^{3X}S/{}^{32}S$ and 3X = 33 or 34) relative to Vienna Canyon Diablo troilite (VCDT). Measurements of $\delta^{34}S$ were calibrated to IAEA, NBS 127 and in-house standards. The 1σ analytical uncertainty on SO_2-based $\delta^{34}S$ measurements was ~0.3‰, while the 1σ analytical uncertainty by SF_6-based $\delta^{34}S$ and $\Delta^{33}S$ measurements was 0.2‰ and 0.005‰, respectively.

Modeling Diagenetic Pyrite Genesis

Following Liu et al. (2020), a diagenetic model was used to model the $\delta^{34}S$ of pyrite at site BB03. This model considers that pyrite is rapidly formed at the sediment surface and is more slowly augmented throughout burial. Thus, a bulk weight-specific rate of pyrite formation below the sediment surface is estimated based on a low CRS content at the surface and a high CRS content at the base of the core. The total pyrite accumulation rate during sediment burial is, therefore, calculated by multiplying the pyrite gradient by the sedimentation rate. Starting at the sediment-water interface, the sediment column is divided into 1 cm intervals. The $\delta^{34}S$ of pyrite at a given depth (*i*) reflects the $\delta^{34}S$ of the overlying pyrite at depth $i-1$ plus the newly-formed pyrite at depth *i* (Equ. 3). Butler et al. (2004) proposed that the $\delta^{34}S$ of pyrite reflects its formation pathway. Pyrite derived from the H_2S pathway ($FeS + H_2S \rightarrow FeS_2 + H_2$; Equ. 4) obtains a mixed $\delta^{34}S$ signal

derived from its constituent FeS and H_2S sources, while pyrite formed by the polysulfide pathway rather records the $\delta^{34}S$ of the precursor polysulfide ($FeS + S_x^{2-} \rightarrow FeS_2 + S_{x-1}^{2-}$; Equ. 5). Consequently, a series of equations were written to simulate the downcore $\delta^{34}S$ evolution of pyrite:

$$m_i \, F^{3X}S_i = m_{i-1} \, F^{3X}S_{i-1} + m_{new} \, F^{3X}S_{new} \quad (3)$$

$$F^{3X}S_{new} = (F^{3X}S_{H2S} + F^{3X}S_{FeS}) / 2 \quad (4)$$

$$F^{3X}S_{new} = F^{3X}S_{polysulfide} \quad (5)$$

where *F* represents fractional isotopic abundances of ^{32}S or ^{34}S (i.e., $F^{3X}S = {}^{3X}S / ({}^{32}S + {}^{34}S)$; 3X = 32 or 34) and *m* represents the molar quantity of pyrite at each depth interval (*i*). The term *new* (i.e., $F^{3X}S_{new}$ and m_{new}) refers to the newly-formed pyrite at depth *i*.

In approximate form, $F^{3X}S$ can be replaced with $\delta^{34}S$ in Equ. 3–5, allowing the $\delta^{34}S$ of pyrite to be calculated via a combination of Equ. 3 with either Equ. 4 or Equ. 5. Where data were unavailable, the $\delta^{34}S_i$ of FeS, H_2S and polysulfide were derived by linear interpolations/extrapolations from the wider $\delta^{34}S$ dataset. Although no H_2S-derived $\delta^{34}S$ data exist below 60 cmbsf, the $\delta^{34}S$ of H_2S is constrained between 4.4 and 21.5‰, enveloped by the highest measured pyrite $\delta^{34}S$ value and the $\delta^{34}S$ of seawater sulfate. Sensitivity tests using these hypothetical end-members alter model outputs by 0–5.7‰. While we explicitly assume that the respective $\delta^{34}S$ values of ZVS and AVS reflect those of solid-phase polysulfide and Fe monosulfide precursors, in reality, however, ZVS includes both elemental sulfur and polysulfide (e.g., Holmkvist et al., 2014). Moreover, the $\delta^{34}S$ value of polysulfides could be higher than assumed due to active, but incomplete, isotope exchange between aqueous sulfide and elemental sulfur (Fig. 3A; Liu et al., 2020). Thus, we stress that our modeled $\delta^{34}S_{py}$ outputs for the H_2S and the polysulfide pathways should be considered as hypothetical maxima and minima, respectively.

In addition to the steady-state consideration presented above, a non-steady-state scenario was also explored. Here, for the sake of simplification, the pyrite pool at each depth is considered a mixture of pyrite inherited from the sediment surface ($\delta^{34}S$ = −30.9‰ at 1 cmbsf) and pyrite formed at depth, each with a $\delta^{34}S$ corresponding to the relevant depth-specific pyrite precursors (Equ. 4–5). Using measured CRS abundances and $\delta^{34}S$ values, the fraction of CRS inherited from the sediment surface can be derived, allowing the downcore variation in this early-formed CRS component to be assessed, thereby disclosing the temporal variation in pyritization at the sediment-water interface. Below 60 cmbsf, the $\delta^{34}S$ value of ZVS is consistently lower than that of co-existing pyrite (Fig. 3A). Considering the polysulfide pathway via Equ. 5, this suggests an early-formed pyrite content lower than 0 μmol g^{-1}. This is not possible, and requires that either (i) the polysulfide pathway was of minor importance below 60 cmbsf, and/or (ii) the $\delta^{34}S$ of polysulfide is much higher than that of ZVS due to an isotopic signal derived largely from elemental sulfur (e.g., Holmkvist et al., 2014). Furthermore, given the lack of H_2S-derived $\delta^{34}S$ data below 60 cmbsf, a constant $\delta^{34}S_{H2S}$ value of 7.7‰ has been assumed, representing an average of the highest measured $\delta^{34}S_{py}$ value (4.4‰) and the deepest measured $\delta^{34}S_{H2S}$ value (11.0‰). Given these uncertainties, the simulation presented in Fig. 4A uses the H_2S pathway (Equ. 4) to predict the early-formed CRS content, while variability in the input $\delta^{34}S$ values of H_2S equates to up to ±11.2 μmol g^{-1} variance in the modeled early-formed CRS content. Some model outputs feature negative contents in Fig. 4A, which are plotted as 0 μmol g^{-1}.

SUPPLEMENTAL DISCUSSION

Low Reactive Iron Content in the Uppermost 40 cm of Core BB03

While non-sulfur-bound reactive Fe is typically more abundant in near-surface than in sub-surface sediments (März et al., 2008; Riedinger et al., 2017; Riedinger et al., 2005), the content of non-sulfur-bound reactive Fe in the upper 40 cm of core BB03 is relatively low (20.9 ± 3.6 μmol g^{-1}, 1σ; Fig. S1F). Interestingly, low reactive Fe contents are also observed in the upper 20 cm of cores BB01 and BB02 (Liu et al., 2020), which, given the different accumulation rates (Table S1), suggests that the relatively low reactive Fe contents seen across the Bornholm Basin reflect reduced Fe input over the last few centuries. Indeed, such a relatively recent decrease in Fe flux is implied by the recognition of a substantial subsurface increase in total Fe content seen at a neighboring site (Kunzendorf and Larsen, 2009). Admittedly, although the low reactive Fe content may have limited the pyrite accumulation in the upper 40 cm of core BB03, it is not expected to have influenced pyrite formation at depth where the reactive Fe content is clearly higher (Fig. S1).

The Effect of Sedimentation Rate on Organic Matter Availability and the H_2S-$\delta^{34}S$ Gradient

Pasquier et al. (2017) argued that sedimentation rate controlled the $\delta^{34}S$ values of pyrite through altered organic matter availability which in turn influenced the cell-specific sulfate reduction rate (csSRR). Although the sedimentation rate at site BB03 is much higher than that of site BB02 (Table S1), the total organic carbon content and $\delta^{13}C_{org}$ are largely similar between the two sites (Figs. S3A–B). This implies that a site-specific difference in the type and reactivity of the bulk organic matter is unlikely. Moreover, while *in vitro* approaches demonstrate csSRR is the key parameter controlling the expression of sulfur isotope fractionation during sulfate reduction, with faster csSRR yielding smaller magnitude sulfur isotope fractionations (Sim et al., 2011;

Leavitt et al., 2013). Such a range in sulfur isotope fractionation is rarely seen in natural environments. For instance, in marine sediments, the generally low levels of metabolizable substrate, combined with its typical recalcitrance, culminate in low csSRR and the broadly uniform expression of large magnitude sulfur isotope fractionation (i.e., > 60‰; Hoehler and Jørgensen, 2013; Jørgensen et al., 2019). Consequently, we suggest that sedimentation rate cannot modulate the inherent metabolic activity of sulfate reducing microorganisms to the extent required to explain the observed $\delta^{34}S$ variability captured by sedimentary pyrite in the Bornholm Basin (Fig. 2B).

Pasquier et al. (2017) and Liu et al. (2019) also argued that sedimentation rate influenced pyrite-$\delta^{34}S$ values through altered porewater communication with the overlying water column, resulting in a modified porewater H_2S-$\delta^{34}S$ gradient. Here, however, we argue that the burial of reactive Fe is an equally important constraint to incorporate within diagenetic models of pyrite formation. For instance, when we apply their previous conceptual models to the Bornholm Basin (e.g., Liu et al., 2019), they produce a steeper H_2S-$\delta^{34}S$ gradient at site BB03 compared to site BB02, owing to the faster sediment accumulation at site BB03 (Table S1). In reality, however, both the H_2S-$\delta^{34}S$ and H_2S concentration profiles are broadly analogous between the two sites (Figs. S3C, S4). Therefore, altered communication between porewater and the overlying water mass cannot readily be invoked to explain the observed pyrite-$\delta^{34}S$ differences (Fig. 2B). Instead, as discussed within the main text, we envisage a sedimentation rate control on subsurface reactive Fe availability as the primary driver of the observed difference in pyrite $\delta^{34}S$ values.

Diagenetic Modeling for the Sulfur Isotopic Composition of Pyrite

Within the accompanying manuscript, a steady-state diagenetic model was employed to simulate the downcore evolution of pyrite-$\delta^{34}S$ values at site BB03 by fixing the initial quantity of

pyrite inherited from the surface, while progressively increasing the pyrite content with depth (cf. Fig. S1C). Following this additive profile (solid line; Fig. 4B), we found a general data-model mismatch whereby, with the exception of sediments found between 200 and 450 cmbsf, the simulated pyrite-$\delta^{34}S$ values were more negative than their measured counterparts (Figs. 4C, S5), demonstrating, in turn, that a steady-state approximation was a poor choice to simulate pyrite genesis in the Bornholm Basin.

Employing a two end-member mixing model suggests that the early-formed pyrite content of sediments from between 50 and 200 cmbsf was much lower than that found in the upper 50 cm of the core and, indeed, those measured in contemporary surficial sediments (Fig. 4A). If the same diagenetic model is re-run in the absence of pyrite formation at the sediment surface (dashed line; Fig. 4B), a reasonable agreement with the measured $\delta^{34}S$ values is achieved between 50 and 200 cmbsf (Fig. 4C). We note that some pyrite-$\delta^{34}S$ values at 60–130 cmbsf are higher than what the model predicts, perhaps signaling that the early-formed surficial pyrite had an even higher $\delta^{34}S$ value than that found today (Liu et al., 2020). This may be due to sediment reworking (Fike et al., 2015) or changes in the upward flux of ^{34}S-enriched H_2S (Jørgensen et al., 2004).

REFERENCES CITED

Andrén, E., Andrén, T., and Sohlenius, G., 2000, The Holocene history of the southwestern Baltic Sea as reflected in a sediment core from the Bornholm Basin: Boreas, v. 29, no. 3, p. 233-250, doi:10.1111/j.1502-3885.2000.tb00981.x.

Andrén, T., et al., 2015, Site M0065, *in* Andrén, T., et al., Proceedings of the Integrated Ocean Drilling Program, Volume 347: College Station, Texas, Integrated Ocean Drilling Program, doi:10.2204/iodp.proc.347.109.2015.

Beulig, F., Røy, H., Glombitza, C., and Jørgensen, B. B., 2018, Control on rate and pathway of anaerobic organic carbon degradation in the seabed: Proceedings of the National Academy of Sciences, v. 115, no. 2, p. 367-372, doi:10.1073/pnas.1715789115.

Beulig, F., Røy, H., McGlynn, S. E., and Jørgensen, B. B., 2019, Cryptic CH_4 cycling in the sulfate-methane transition of marine sediments apparently mediated by ANME-1 archaea: The ISME Journal, v. 13, no. 2, p. 250-262, doi:10.1038/s41396-018-0273-z.

Butler, I. B., Böttcher, M. E., Rickard, D., and Oldroyd, A., 2004, Sulfur isotope partitioning during experimental formation of pyrite via the polysulfide and hydrogen sulfide pathways: implications for the interpretation of sedimentary and hydrothermal pyrite isotope records: Earth and Planetary Science Letters, v. 228, no. 3, p. 495-509, doi:10.1016/j.epsl.2004.10.005.

Canfield, D. E., Raiswell, R., and Bottrell, S. H., 1992, The reactivity of sedimentary iron minerals toward sulfide: American Journal of Science, v. 292, no. 9, p. 659-683, doi:10.2475/ajs.292.9.659.

Cline, J. D., 1969, Spectrophotometric determination of hydrogen sulfide in natural waters: Limnology and Oceanography, v. 14, no. 3, p. 454-458, doi:10.4319/lo.1969.14.3.0454.

Fike, D. A., Bradley, A. S., and Rose, C. V., 2015, Rethinking the ancient sulfur cycle: Annual Review of Earth and Planetary Sciences, v. 43, no. 1, p. 593-622, doi:10.1146/annurev-earth-060313-054802.

Findlay, A. J., Gartman, A., MacDonald, D. J., Hanson, T. E., Shaw, T. J., and Luther, G. W., 2014, Distribution and size fractionation of elemental sulfur in aqueous environments: the Chesapeake Bay and Mid-Atlantic Ridge: Geochimica et Cosmochimica Acta, v. 142, p. 334-348, doi:10.1016/j.gca.2014.07.032.

Flury, S., Røy, H., Dale, A. W., Fossing, H., Tóth, Z., Spiess, V., Jensen, J. B., and Jørgensen, B. B., 2016, Controls on subsurface methane fluxes and shallow gas formation in Baltic Sea sediment (Aarhus Bay, Denmark): Geochimica et Cosmochimica Acta, v. 188, p. 297-309, doi:10.1016/j.gca.2016.05.037.

Fossing, H., and Jørgensen, B. B., 1989, Measurement of bacterial sulfate reduction in sediments: evaluation of a single-step chromium reduction method: Biogeochemistry, v. 8, no. 3, p. 205-222, doi:10.1007/BF00002889.

Henkel, S., Kasten, S., Poulton, S. W., and Staubwasser, M., 2016, Determination of the stable iron isotopic composition of sequentially leached iron phases in marine sediments: Chemical Geology, v. 421, p. 93-102, doi:10.1016/j.chemgeo.2015.12.003.

Hilligsøe, K. M., Jensen, J. B., Ferdelman, T. G., Fossing, H., Lapham, L., Røy, H., and Jørgensen, B. B., 2018, Methane fluxes in marine sediments quantified through core analyses and seismo-acoustic mapping (Bornholm Basin, Baltic Sea): Geochimica et Cosmochimica Acta, v. 239, p. 255-274, doi:10.1016/j.gca.2018.07.040.

Hoehler, T. M., and Jørgensen, B. B., 2013, Microbial life under extreme energy limitation: Nature Reviews Microbiology, v. 11, no. 2, p. 83-94, doi:10.1038/nrmicro2939.

Holmkvist, L., Kamyshny Jr, A., Bruechert, V., Ferdelman, T. G., and Jørgensen, B. B., 2014, Sulfidization of lacustrine glacial clay upon Holocene marine transgression (Arkona Basin, Baltic Sea): Geochimica et Cosmochimica Acta, v. 142, p. 75-94, doi:10.1016/j.gca.2014.07.030.

Jensen, J. B., Moros, M., Endler, R., and Members, I. E., 2017, The Bornholm Basin, southern Scandinavia: a complex history from Late Cretaceous structural developments to recent sedimentation: Boreas, v. 46, no. 1, p. 3-17, doi:10.1111/bor.12194.

Jørgensen, B. B., Böttcher, M. E., Lüschen, H., Neretin, L. N., and Volkov, I. I., 2004, Anaerobic methane oxidation and a deep H_2S sink generate isotopically heavy sulfides in Black Sea sediments: Geochimica et Cosmochimica Acta, v. 68, no. 9, p. 2095-2118, doi:10.1016/j.gca.2003.07.017.

Jørgensen, B. B., Findlay, A. J., and Pellerin, A., 2019, The biogeochemical sulfur cycle of marine sediments: Frontiers in Microbiology, v. 10:849, doi:10.3389/fmicb.2019.00849.

Kunzendorf, H., and Larsen, B., 2009, Environmental changes in the Bornholm Basin as deduced from the geochemistry of short and long sediment cores: Baltica, v. 22, no. 2, p. 101-110.

Leavitt, W. D., Halevy, I., Bradley, A. S., and Johnston, D. T., 2013, Influence of sulfate reduction rates on the Phanerozoic sulfur isotope record: Proceedings of the National Academy of Sciences, v. 110, no. 28, p. 11244-11249, doi:10.1073/pnas.1218874110.

Liu, J., Pellerin, A., Antler, G., Kasten, S., Findlay, A. J., Dohrmann, I., Røy, H., Turchyn, A. V., and Jørgensen, B. B., 2020, Early diagenesis of iron and sulfur in Bornholm Basin sediments: The role of near-surface pyrite formation: Geochimica et Cosmochimica Acta, v. 284, p. 43-60, doi:10.1016/j.gca.2020.06.003.

Liu, X., Fike, D., Li, A., Dong, J., Xu, F., Zhuang, G., Rendle-Bühring, R., and Wan, S., 2019, Pyrite sulfur isotopes constrained by sedimentation rates: Evidence from sediments on the East China Sea inner shelf since the late Pleistocene: Chemical Geology, v. 505, p. 66-75, doi:10.1016/j.chemgeo.2018.12.014.

März, C., Hoffmann, J., Bleil, U., De Lange, G., and Kasten, S., 2008, Diagenetic changes of magnetic and geochemical signals by anaerobic methane oxidation in sediments of the Zambezi deep-sea fan (SW Indian Ocean): Marine Geology, v. 255, no. 3, p. 118-130, doi:10.1016/j.margeo.2008.05.013.

Ono, S., Keller, N. S., Rouxel, O., and Alt, J. C., 2012, Sulfur-33 constraints on the origin of secondary pyrite in altered oceanic basement: Geochimica et Cosmochimica Acta, v. 87, p. 323-340, doi:10.1016/j.gca.2012.04.016.

Pasquier, V., Sansjofre, P., Rabineau, M., Revillon, S., Houghton, J., and Fike, D. A., 2017, Pyrite sulfur isotopes reveal glacial−interglacial environmental changes: Proceedings of the National Academy of Sciences, v. 114, no. 23, p. 5941-5945, doi:10.1073/pnas.1618245114.

Pellerin, A., Antler, G., Røy, H., Findlay, A., Beulig, F., Scholze, C., Turchyn, A. V., and Jørgensen, B. B., 2018, The sulfur cycle below the sulfate-methane transition of marine sediments: Geochimica et Cosmochimica Acta, v. 239, p. 74-89, doi:10.1016/j.gca.2018.07.027.

Poulton, S. W., and Canfield, D. E., 2005, Development of a sequential extraction procedure for iron: implications for iron partitioning in continentally derived particulates: Chemical Geology, v. 214, no. 3-4, p. 209-221, doi:10.1016/j.chemgeo.2004.09.003.

Riedinger, N., Brunner, B., Krastel, S., Arnold, G. L., Wehrmann, L. M., Formolo, M. J., Beck, A., Bates, S. M., Henkel, S., and Kasten, S., 2017, Sulfur cycling in an iron oxide-dominated, dynamic marine depositional system: The Argentine continental margin: Frontiers in Earth Science, v. 5:33, doi:10.3389/feart.2017.00033.

Riedinger, N., Pfeifer, K., Kasten, S., Garming, J. F. L., Vogt, C., and Hensen, C., 2005, Diagenetic alteration of magnetic signals by anaerobic oxidation of methane related to a change in sedimentation rate: Geochimica et Cosmochimica Acta, v. 69, no. 16, p. 4117-4126, doi:10.1016/j.gca.2005.02.004.

Sim, M. S., Bosak, T., and Ono, S., 2011, Large Sulfur Isotope Fractionation Does Not Require Disproportionation: Science, v. 333, no. 6038, p. 74-77, doi:10.1126/science.1205103.

Slotznick, S. P., Sperling, E. A., Tosca, N. J., Miller, A. J., Clayton, K. E., van Helmond, N. A. G. M., Slomp, C. P., and Swanson-Hysell, N. L., 2020, Unraveling the Mineralogical Complexity of Sediment Iron Speciation Using Sequential Extractions: Geochemistry, Geophysics, Geosystems, v. 21, no. 2, p. e2019GC008666, doi:10.1029/2019gc008666.

SUPPLEMENTAL TABLE AND FIGURES

Table S1. Geographical, physical and geochemical details pertaining to the four sites examined/discussed within the Bornholm Basin. HML and SMT abbreviate Holocene mud layer and sulfate-methane transition, respectively. Site-specific sedimentation rate is denoted ω, while average $\delta^{34}S_{CRS}$ signals the average $\delta^{34}S$ value of Holocene-aged chromium reducible sulfur. Data are sourced from Andrén et al. (2015), Beulig et al. (2018) and Liu et al. (2020).

Site	Latitude / longitude	Water depth (m)	HML (m)	SMT (mbsf)	ω (cm ka^{-1})	Average $\delta^{34}S_{CRS}$ (‰, VCDT; ±1σ)
BB03	55°28.119′N / 15°28.647′E	84	9.6	0.4	113	−14 ± 12
BB01	55°22.922′N / 15°27.675′E	96	5.5	0.6	65	−22 ± 5
BB02	55°23.281′N / 15°28.004′E	96	4.5	0.7	53	−32 ± 4
BB05	55°24.418′N / 15°28.550′E	95	4.2	3.7	49	−37 ± 3

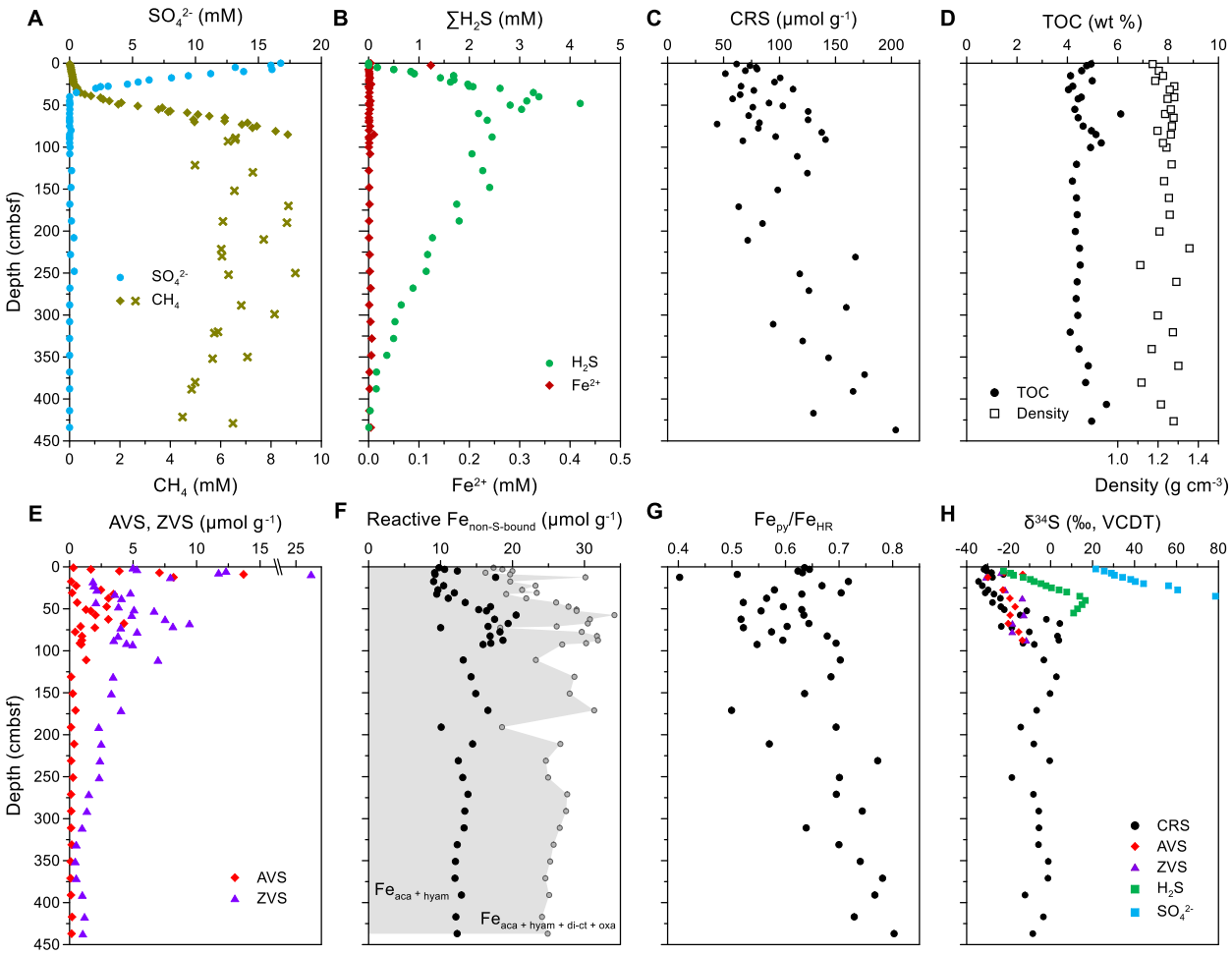

Figure S1. Geochemical depth profiles for site BB03 in the Bornholm Basin, Baltic Sea. (A) Porewater sulfate and methane (Beulig et al., 2018). Methane data below 85 cmbsf are compromised by methane loss and, therefore, are considered minimum estimates denoted by a separate symbol. (B) Porewater sulfide (Pellerin et al., 2018) and ferrous iron. (C) Chromium reducible sulfur (CRS, predominantly pyrite). (D) Total organic carbon (TOC; Beulig et al., 2018) and wet sediment density. (E) Acid volatile sulfur (AVS) and zero-valent sulfur (ZVS). (F) Non-sulfur-bound reactive iron. (G) Extent of pyritization of the highly reactive iron pool (Fe_{py}/Fe_{HR}). (H) The sulfur isotopic composition ($\delta^{34}S$) of various color-coded chemical species.

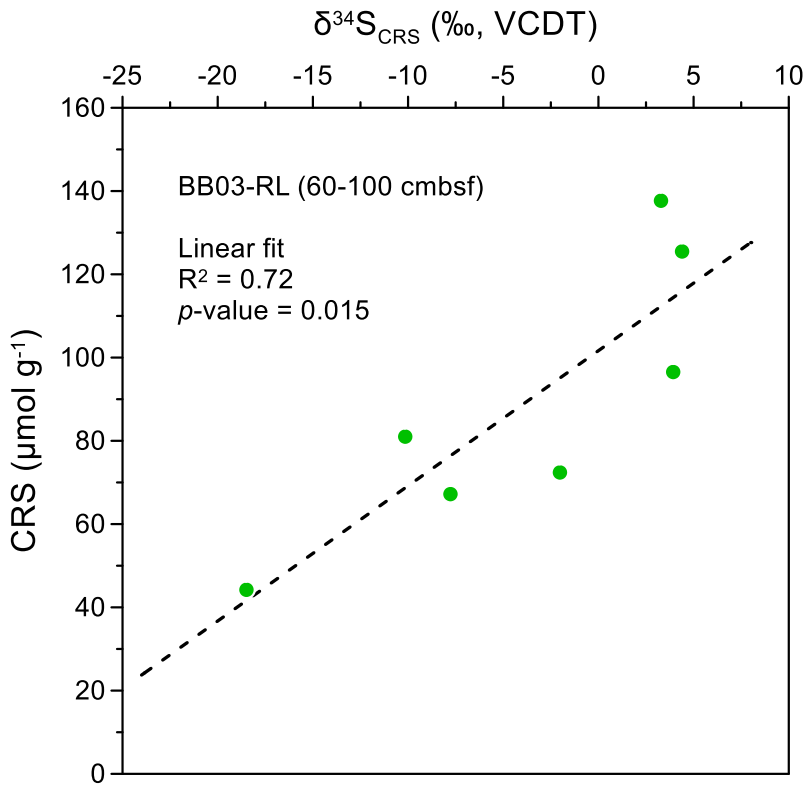

Figure S2. Chromium reducible sulfur (CRS) abundance *versus* its $\delta^{34}S$ value between 60 and 100 cmbsf at site BB03. The observed positive correlation implies that bulk CRS measurements integrate time-specific, and progressively ^{32}S-depleted, generations of pyrite. Consequently, the scatter within the CRS dataset (Fig. S1C) may reflect non-steady-state pyrite genesis.

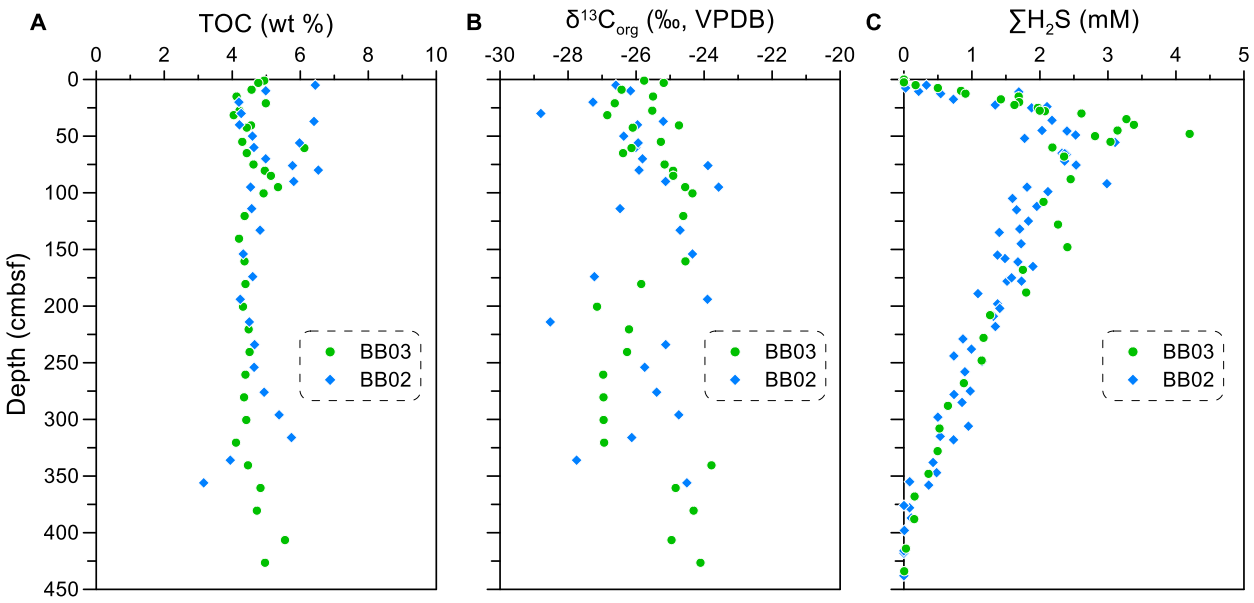

Figure S3. Comparison of geochemical depth profiles obtained from sites BB03 and BB02. (A) Total organic carbon (TOC) content. (B) Organic carbon isotopic composition. (C) Porewater sulfide concentration. Data from Beulig et al. (2018, 2019), Pellerin et al. (2018) and Liu et al. (2020).

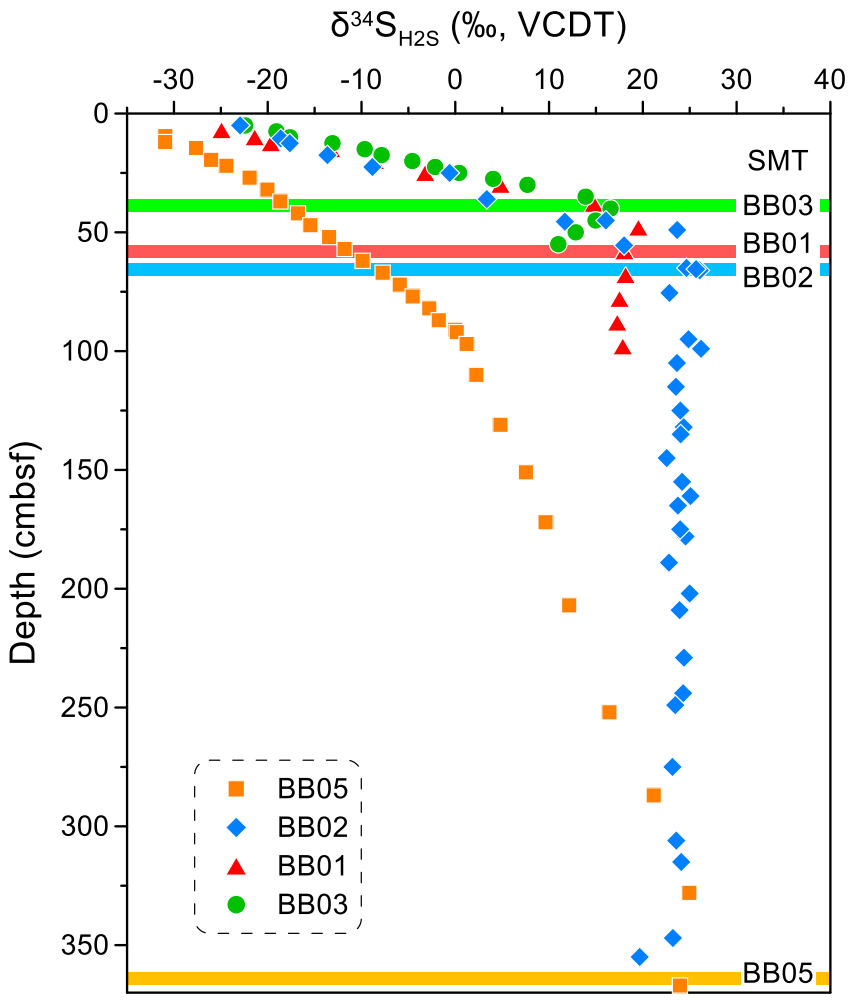

Figure S4. Sulfide-derived porewater $\delta^{34}S$ profiles obtained from each of the four examined sites within the Bornholm Basin. Here, symbols and horizontal bars, representing the depth of the sulfate-methane transition (SMT), are color-coded to distinguish between sites. Data from sites BB01 (red), BB02 (blue) and BB05 (orange) are from Liu et al. (2020).

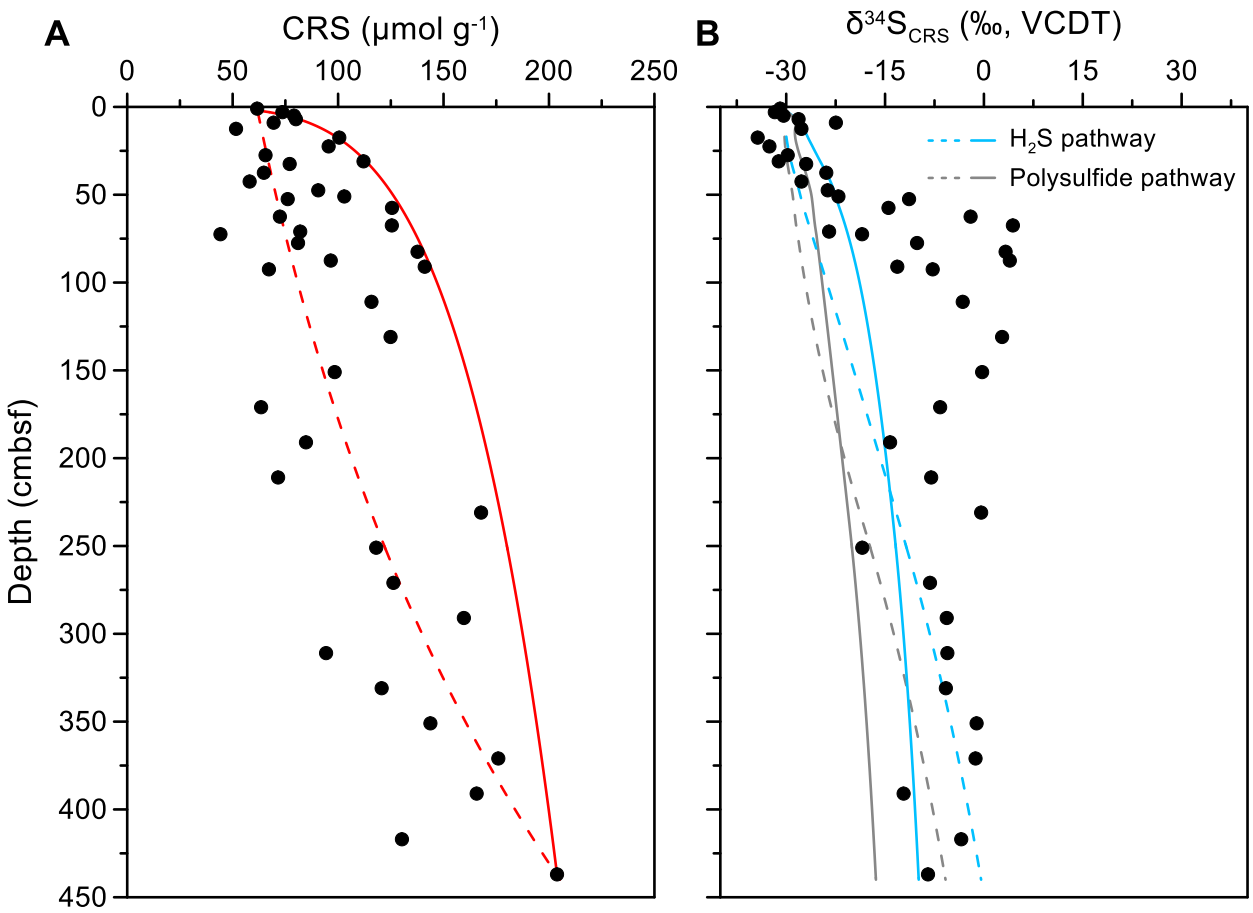

Figure S5. Sensitivity test of the modeled pyrite $\delta^{34}S$ values to changes in the gradient of the pyrite content. (A) The red lines illustrate the variable depth-specific rates of pyrite formation used within the model. (B) The grey and blue lines denote the modeled $\delta^{34}S_{CRS}$ values formed via either the polysulfide or the H_2S pathways. The solid and dashed lines correspond to the assumed gradient of the pyrite content in panel A. A non-linear profile of pyrite accumulation with depth makes a minor change in the output $\delta^{34}S$.